Spatial blurring in Laser speckle imaging in Inhomogeneous systems

Luka Vitomir

March 2017
Wageningen University

Spatial blurring in Laser speckle imaging in Inhomogeneous systems

Luka Vitomir
930118896070

M.Sc. Thesis
Physical Chemistry and Soft Matter group
PCC-80436

Wageningen University and Research Center

Helix 124, Stippeneng 4, 6709 WE
Wageningen

Supervisors: dr.ir. Joris Sprakel
dr.ir. Jasper van der Gucht

Table of contents

Abstract

Laser speckle imaging (LSI) has developed into a versatile tool to image dynamical processes in turbid media, such as subcutaneous blood perfusion and structural dynamics in materials. In performing these experiments, the diffusive nature of photon paths prior to detection, leads to an inherent spatial convolution of inhomogeneous structures and dynamics in the final images. In this paper we derive a theory for LSI in the Rayleigh regime using the diffusion approximation, to evaluate these spatial averages and their effect on the interpretation of LSI results. We first construct an enhanced backscatter setup and confirm the validity of Rayleigh theory. Next, using a random walk formalism, we derive and calculate the photon density distribution for a semi-infinite homogeneous system, and verify the results with Monte-Carlo simulations. Finally, we derive a model for inhomogeneous systems, that describes the dependence of the electric field correlation function, on sample structure and transport mean free path. The predictions are confirmed by simulating a sample, consisting of a convective layer embedded within a diffusive slab, and showing that the contribution of the convective layer to de-correlation in LSI depends non-linearly on layer position, imaging wavelength, and exponential decay time constant.

1. Introduction

Laser speckle imaging (LSI) is a light-based imaging technique widely used for non-invasive characterization of soft and turbid media.[1] The ability to probe internal dynamic processes without introducing external disturbances, combined with its cost-effectiveness, makes LSI highly suitable for scientific and industrial purposes. Amongst many other fields, LSI is widely applied in biomedicine and medical imaging, materials science, food technology and physical chemistry.[2–8] To exemplify, several of LSI's many uses include subcutaneous blood-flow monitoring, imaging of paint-drying processes with high spatial resolution, mechanical mapping of visco-elastic moduli in bio-materials, and analysis of surface roughness in plastic packaging films.[9–12] Recently, LSI has even been applied to the study of cutaneous wound progression.[13] The latter study highlights the potential of LSI to investigate multi time-scale dynamics in inhomogeneous systems, such as biological tissue or self-healing materials.

The development of LSI technology and the widening array of its applications have been stimulated by the underlying theoretical progress with regards to describing light propagation in turbid systems. LSI is based on the analysis of intensity fluctuations resulting from interference of photon paths within a sample. Depending on the physical, chemical, and structural properties of a sample under illumination, photons may be either absorbed, transmitted, or scattered back through the entry plane.[14] LSI typically works in the multiple-scattering regime, meaning that only the photons that have spent sufficient time within the sample are analyzed. The light scattered back from the sample surface is polarization-filtered to ensure that the detected photons have lost their polarization, and consequently, have probed the sample to a sufficient extent. The selected photons are then imaged onto a CCD detector, whose pixels register the intensity fluctuations. The propagation of photons within a diffusive sample can be described as a chain of sequential scatterings, resulting from the traveling photons bouncing off of the system constituents.[15] The distance between the scatterings is known as the mean free path, l, which has a Gaussian distribution and depends on imaging wavelength and sample parameters. Since LSI is done in the multiple-scattering limit, the primary quantity of interest is the transport mean free path, l^*. This is the distance traveled by a photon before it loses its polarization. The relation between l and l^* depends on the type of scattering process. Once in the sample, the photon paths undergo interference upon crossing each other. This causes the CCD pixels to register regions of enhanced or reduced intensity, also known as speckles. Depending on the internal dynamics of the sample, this speckle pattern will or will not fluctuate.[16] By measuring the self-correlation of speckle patterns, one can determine quantities characterizing the type and rate of internal dynamic processes.[17] Here, it is appropriate to introduce the intensity correlation function, $g_2(\tau)$, and the electric field correlation function, $g_1(\tau)$.[18] They quantify the intensity and electric field self-correlation, respectively, and are a convenient way of quantifying fluctuating light patterns. They are connected by the Siegert relation: $g_2(\tau) = 1 + g_1(\tau)^2$. When photons follow scattering trajectories in a dynamic, Brownian medium, it is necessary to obtain a series of sequential speckle images that will enable calculation of $g_1(\tau)$ and $g_2(\tau)$.[19] By choosing an exponential-decay time constant, τ, which is the imaging frame interval, one can choose the time-scale of correlation measurements, and thereby selectively measure fast or slow processes. In samples with a homogeneous composition, photons of the same wavelength will have the same l^* in every region within the sample. Thus every region will represent the same scattering process, and have the same contribution to the measured speckle pattern.[20] However, for inhomogeneous samples, the speckle pattern depends on the photon density distribution.[21] The latter gives the probability distribution of photons probing different regions within a sample. Since photons of different wavelength will probe the sample, including inhomogeneous regions, to a varying extent, they will also contribute differently to the measured speckle correlation pattern. Consequently, LSI measurements performed on inhomogeneous samples actually represent averages, resulting from spatial convolution of dynamic processes and structural parameters.[22,23] In order to properly apply LSI for imaging of multi-scale dynamic processes in inhomogeneous systems, it is necessary to treat spatial averaging in

the context of de-correlation.

In this paper, we investigate the causes of resolutional blurring in LSI measurements on inhomogeneous systems. First, we experimentally validate Rayleigh theory by measuring the wavelength-dependence of photon mean free path. Next, using the diffusion approximation, we derive a random walk model for the calculation of photon density distributions, for a semi-infinite slab with varying degrees of inhomogeneity.[21,24] We verify the results for a homogeneous sample with Monte-Carlo simulations. Finally, we simulate LSI measurements for two different conformations of an inhomogeneous system, consisting of a convective layer embedded in a diffusive slab, and analyze the results within the framework of our model.

2. Rayleigh theory

We base our theory of LSI in inhomogeneous systems on the fact that, for the Rayleigh regime, where $\lambda > r_{scatterer}$, different wavelengths have different photon density distribution profiles within a sample. This relies on the assumption of a wavelength-dependent transport mean free path. The transport mean free path in the Rayleigh regime is given by:

$$l^* = \frac{3\lambda^4}{\left(128\pi^5 a^6 \rho_{nr}\right)\left(\frac{m^2-1}{m^2+2}\right)^2 \langle 1 - cos\theta \rangle} \tag{1}$$

Here, λ is the imaging wavelength, a is the particle radius, ρ_{nr} the number density, and $m = \frac{n_p}{n_m}$, where n_p and n_m are the refractive indices of particle and medium, respectively. In the Rayleigh regime, l^* and l are related by $l^* = \frac{l}{1-\langle cos\phi \rangle}$. In order to confirm this fundamental assumption, we had to verify the predictions of Rayleigh theory. For this purpose we constructed an enhanced back-scatter setup, shown in figure (1a). This method takes advantage of the weak-localization effect of light.[25] In a sample illuminated by a pencil-beam orthogonally to its surface, photons will enter the sample and undergo a random walk. Some of them will end their walk at the entry surface and therefore be emitted, i.e. back-scattered. If we regard the latter path as the forward-path, then we can also define a time-reversed path. Here, a photon takes the same route within the sample as the photon on the forward path, but with an opposite direction, and thus opposite entry- and exit-points. A pair of forward and time-reversed paths interfere constructively. The probability of a back-scatter photon path will be highest in and near the beam center, while gradually decaying in the radial direction. Therefore, in the region in and near the beam-center, forward and time-reversed paths will interfere most strongly. By measuring the shape of the radial intensity decay curve for a particular wavelength, one can estimate the corresponding transport mean free path. We measured the transport mean free path for a

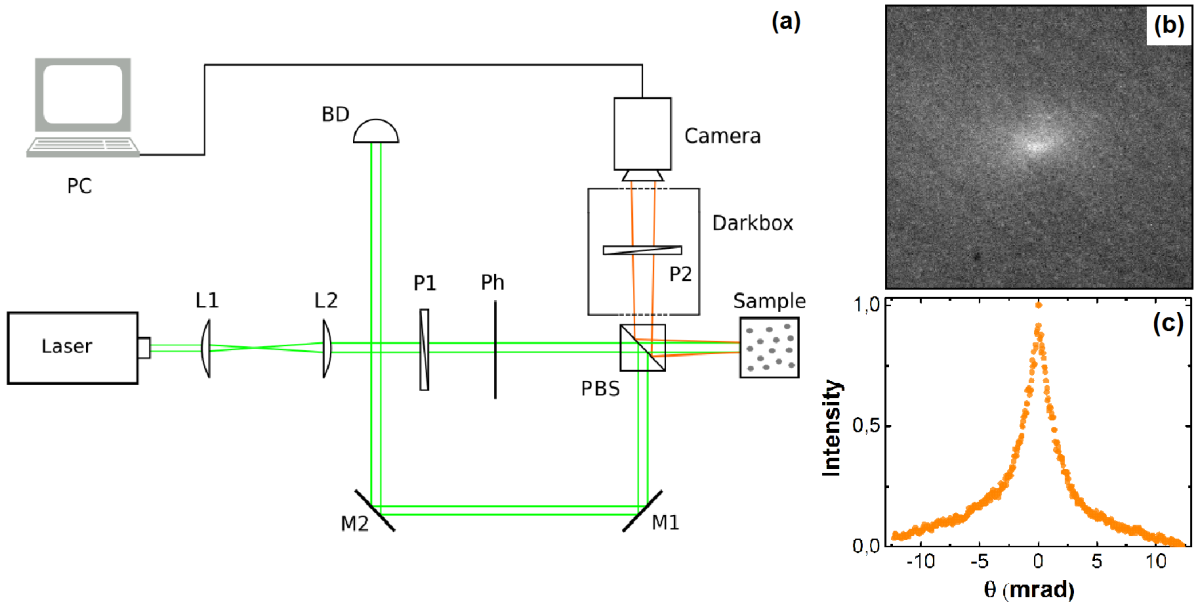

Figure 1. **(a)** Enhanced backscatter setup used for transport mean free path measurements: (L_1, L_2) lens 1 and 2 of beam-expander, (P_1, P_2) polarizers, (P_h) pinhole, (PBS) pellicle beam-splitter, (M_1, M_2) mirrors, (BD) beam-dump; **(b)** Weak-localization effect of light, and the resulting enhanced back-scatter cone; **(c)** Radial intensity profile for $\lambda = 660\ nm$.

turbid polystyrene sample satisfying the criteria for Rayleigh scattering, for four wavelengths in the visible spectrum, and compared the results with the theoretical predictions. Figure (2) shows a comparison between experimental results and theory. We used number density as fitting parameter since it was approximated on the basis of composition. The ρ_{nr}-value minimizing

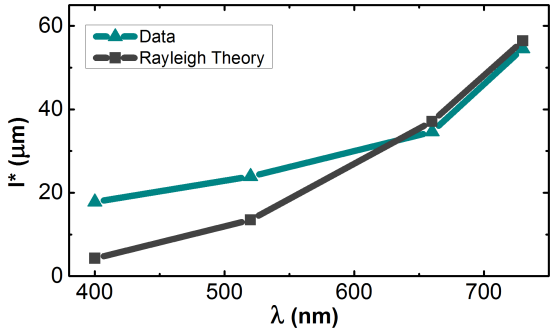

Figure 2. Transport mean free path as a function of wavelength, for the Rayleigh regime.

residual error was found to be $1 \cdot 10^{20}\ m^{-3}$, which agrees within acceptable bounds with the estimated value of $1.7 \cdot 10^{20}\ m^{-3}$. A disagreement can be noted between data and theory at 405 and 520 nm. This can be explained by the high mass fraction of the suspension, $\phi = 0.45$. In dense environments, photons with wavelengths approaching the lower end of the visible spectrum will interact on the course of small distances between particles. Consequently, the shorter-wavelength photons probing such small length scales will give rise to inter-particle interference.[26] We have assumed isotropic scattering, the requirements for which might not be satisfied for short wavelengths in this sample. This alters the contribution of the structure factor $S(q)$, which describes the amplitude and phase of a scattered wave, to our model, and consequently affects calculation of the transport mean free path. Aside from the discrepancy at short wavelengths, the data and theory demonstrate significant agreement.

3. LSI theory

In the previous sections, we outlined the concept of Rayleigh scattering and light propagation in diffusive, turbid systems. To understand de-correlation in LSI measurements, we start by considering a slab of thickness L (figure 3). Photons enter the

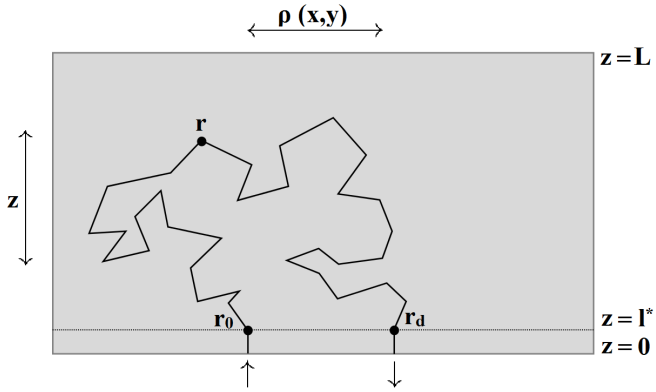

Figure 3. A back-scatter trajectory: r_0 and r_d are the entry and exit points, respectively, and (r) is the location of a scattering event on the photon path. The random walk is assumed to start at a depth of one transport mean free path. The exit plane is also located at $z = l^*$, satisfying the extrapolated boundary condition.

turbid sample at r_0, and undergo a sequence of scattering events before leaving the sample at r_d. In order to calculate the electric-field correlation function as measured with a CCD pixel at r_d, we start with an expression for the electric field $E(t)$, resulting from all photon paths at time t ending at r_d. The total electric field at r_d is:

$$E(t) = \sum_p E_p e^{i\phi_p(t)} \tag{2}$$

where E_p is the amplitude of the electric field from path p, and $\phi_p(t)$ is the phase shift at time t. The phase-shift quantifies the phase difference of a photon at points r_0 and r_d, and is given by:

$$\phi_p(t) = k_0 s(t) = \sum_{i=0}^{N} k_i(t) \cdot [r_{i+1}(t) - r_i(t)] \tag{3}$$

where $k_0 = \frac{2\pi n_p}{\lambda}$ is the wave vector, and $s(t)$ is the total path-length at time t. The electric field autocorrelation function can then be written as a weighted average of the fields at time $t = (0,t)$, and expanded using (2):

$$g_1(t) = \frac{1}{|E|^2}\langle E(0)E^*(t)\rangle \tag{4}$$

$$= \frac{1}{\langle I\rangle}\sum_{p,p'} E_p E_{p'} \langle exp(i[\phi_p(0) - \phi_{p'}])\rangle \tag{5}$$

$$= \sum_p \frac{\langle I_p\rangle}{\langle I\rangle}\langle exp(-i[\phi_p(t) - \phi_p(0)])\rangle \tag{6}$$

The change of summation index from (5) to (6) stems from the fact that terms with $p \neq p'$, which represent different spatial paths, interfere destructively and thus do not contribute to the correlation. The phase shift can then be calculated as the phase difference at time $t = (0,t)$, and expanded with (3):

$$\Delta\phi_p(t) = \phi_p(t) - \phi_p(0) \tag{7}$$

$$= \sum_{i=0}^{N} k_i(t) \cdot [r_{i+1}(t) - r_i(t)] - \sum_{i=0}^{N} k_i(0) \cdot [r_{i+1}(0) - r_i(0)] \tag{8}$$

$$= \sum_{i=1}^{N} k_i \cdot [\Delta r_{i+1}(t) - \Delta r_i(t)] \tag{9}$$

$$= \sum_{i=1}^{N} q_i \cdot \Delta r_i(t) \tag{10}$$

Here, the summation is done over the scattering events N from path p. Equation (10) expresses the phase-shift as a function of the scattering vector and displacement between scattering events $(i, i-1)$, given respectively by $q_i = k_i - k_{i-1}$ and $\Delta r_i = r_i - r_{i-1}$.

LSI is typically used to study Brownian or ballistic dynamics of turbid media, i.e. to probe particle motion, convective flows or mechanical strains. As such, displacement of the scatterers can be caused by any combination of different underlying dynamics. To calculate the phase-shift resulting from a mechanical strain - i.e. a deformation field, we use (9). Equation (10) is used when the only cause of displacement is Brownian motion. For systems exhibiting both a deformation field and thermal fluctuations we can write $\Delta r_i = \Delta r_i^B + u_i$, where Δr_i and Δr_i^B are the deformation and thermal contribution to the displacement, and u_i is the displacement field. Then substituting this into (10) and using (9) gives the phase shift:

$$\Delta\phi_p(t) = \sum_{i=1}^{N} (q_i \cdot \Delta r_i^B(t) + k_i \cdot [u_{i+1}(t) - u_i(t)]) \tag{11}$$

We will now explore the effect of Brownian motion and deformation fields on the field correlation. To illustrate the concept, we first consider a scenario in which displacement of the scatterers is caused only by homogeneous Brownian motion, and there is no ballistic motion or externally applied strain. This model is relevant when using LSI for micro-mechanical mapping of samples in their quiescent state. In this case, the phase shift is given by (10). For random thermal motion, all the Δr_i are fluctuating variables, and for long paths with large N, $\Delta\phi(t)$ becomes a Gaussian random variable. Thus, we can reformulate the expression for the phase-shift as defined in (3), to represent the probability density function of a Gaussian:

$$\langle e^{-i\Delta\phi_p(t)}\rangle = e^{-\frac{1}{2}\langle\Delta\phi_p(t)^2\rangle} \tag{12}$$

This can be reasoned by noting that the average on the left is over a Gaussian distribution. Then, integrating the right part of (12) over all photon paths p to get the total phase shift corresponds to taking the Fourier transform of a Gaussian, which is a Gaussian in itself. Using (10), the average of the phase shift can be written as:

$$\langle \Delta\phi_p(t)^2 \rangle = \sum_{i=1}^{N} \langle (q_i \cdot \Delta r_i(t))^2 \rangle \tag{13}$$

$$= \frac{1}{3} \langle q^2 \rangle \sum_{i=1}^{N} \langle \Delta r_i(t)^2 \rangle \tag{14}$$

where it is assumed that the displacement Δr_i, and the scattering vector q_i, are uncorrelated. In (14), the average of the scattering vector q_i is weighted by the form factor $\langle 1 - cos\theta \rangle$. The form factor is a measure of the amplitude of a scattered wave, and depends on the spatial density distribution of the scatterer around its center of mass. The average in (14) can then be written as:

$$\langle q^2 \rangle = 2k_0^2 \frac{l}{l*} \tag{15}$$

where the scattering vector is a function of the wave vector, and the ratio of the mean free path to the transport mean free path. For this model, we have assumed l and l^* to have a Gaussian distribution. Then, we can write the mean-squared displacement of a scatterer as:

$$\langle (\Delta r_i(t)^2 \rangle = \int \langle \Delta r(r,t)^2 \rangle P_p(r,i) dr \tag{16}$$

Here, $\langle \Delta r(r,t)^2 \rangle$ is the mean-squared displacement at point r, and $P_p(r,i)$ is the probability that the random walk p passes through (r) after i steps. The effective mean-squared displacement is thus written as an integral of the product of the probability function $P_p(r,i)$, and local mean-squared displacement, over all sample points r. To calculate the phase-shift, we re-write (14) using (15) and (16). This gives:

$$\langle \Delta\phi_p(t)^2 \rangle = \frac{2}{3} k_0^2 \frac{s}{l*} \int \langle \Delta r(r,t)^2 \rangle \rho_N(r) dr \tag{17}$$

Here, N is the number of scattering events of path p, and $s = Nl$ is the corresponding path-length. We write the probability density of photons with path-length s crossing point r on their path, by interchanging the sum over scattering events N with an integral:

$$\rho_N(r) = \frac{1}{N} \sum_{i=1}^{N} P_p(r,i) \tag{18}$$

$$\approx \frac{1}{s} \int_0^s P_s(r,n) dn \tag{19}$$

The latter form in equation (19) is valid for paths significantly longer than the mean free path, which corresponds to the multiple scattering limit in LSI. Integrating $\rho_N(r)$ over all sample points r gives us $P(s)$, the path-length probability distribution. Using $P(s)$, we obtain an expression for the electric field correlation function of a Brownian system:

$$g_1(\tau) = \int_0^\infty P(s) exp\Big[-\frac{k_0^2}{3} \frac{s}{l*} \bar{\Gamma}_B \Big] ds \tag{20}$$

Here, $\bar{\Gamma}_B$ expresses the convolution of the spatial density of diffusion paths $\rho_s(r)$, with the mean-squared displacement at point r, attributable to Brownian motion. It is given by:

$$\bar{\Gamma}_B = \int \langle \Delta r(r,t)^2 \rangle \rho_s(r) dr \tag{21}$$

In the case of homogeneous Brownian motion with no thermal gradients, $\rho_s(r)$ will have no effect on the measured de-correlation, and the integral in (21) will reduce to the expression for the mean-squared displacement.

When a system, besides Brownian motion, exhibits also a deformation field - i.e. a mechanical strain or pressure gradient, a modified derivation is required. Here we use the second term in (11), which is the contribution to the phase-shift arising from

the displacement field difference at scattering events $(i, i+1)$. By assuming that the displacement field varies slowly between two scattering events, we can use a Taylor expansion of $u(r)$, which gives:

$$\Delta\phi(t) = \sum_{i=1}^{N} k_i \cdot (l_i \cdot \nabla) u(r_i) \tag{22}$$

$$= \sum_{i=1}^{N} k l_i e_i \cdot (e_i \cdot \nabla) u(r) \tag{23}$$

Here, $l_i = l_i e_i$ is the vector from scattering event i to scattering event j, l_i is the mean free path at event i, and e_i is the unit vector in the corresponding scattering direction. The phase difference resulting from the deformation field can also be written as a function of the scattering and strain tensors:

$$\Delta\phi(t) = k \sum_{i=1}^{N} l_i \sum_{m,n} A_{mn}(i) \varepsilon_{mn}(r_i) \tag{24}$$

where

$$A_{mn}(i) = e_{im} e_{in} \tag{25}$$

is the scattering tensor of the i-th scattering event and

$$\varepsilon_{mn} = \frac{1}{2}\Big(\frac{\partial u_m}{\partial r_n} + \frac{\partial u_n}{\partial r_m}\Big) \tag{26}$$

is the strain tensor. The scattering tensor is composed of the unit vectors for scattering event i, along the displacement field axes, (m,n). The strain tensor gives the variation of the displacement field components (u_m, u_n) along the axes (n,m), respectively. The strain tensor is directly connected with many physical quantities of interest. For solids, $E\varepsilon_{mn}^2$, where E is Young's modulus, is a measure for the deformation energy, whereas for liquids, $\eta\varepsilon_{mn}^2$, where η is viscosity, is a measure for the dissipated energy. For a static mechanical deformation, calculation of the strain tensor is simplified since the pressure gradient does not vary in time. However, for a shearing layer, the strain tensor has a non-vanishing time derivative and is more conveniently expressed as a strain rate tensor.

To arrive at the correct expression for the total phase shift in a deformation field, we again use the fact that for many scattering events, the variable $\Delta\phi$ is a random Gaussian variable, so that we can write:

$$\langle exp(-i\Delta\phi_p(t))\rangle = exp\Big(-\frac{1}{2}[\langle\Delta\phi_p(t)^2\rangle - \langle\Delta\phi_p(t)\rangle^2]\Big) \tag{27}$$

It was shown in[24,27] that the phase-shift for a system exhibiting a deformation field can be written as:

$$\langle\Delta\phi_p^2\rangle - \langle\Delta\phi_p\rangle^2 = \beta l^2 k_0^2 \sum_{i=1}^{N} \Big(\langle(\nabla\cdot u_i)^2\rangle + 2\sum_{m,n}\langle\varepsilon_{m,n}^2(r_i)\rangle\Big) \tag{28}$$

We see that the phase-shift is a function of mean free path l, wave-vector k_0, the divergence of the displacement field, and the strain tensor. β is a constant that depends on the nature and distribution of scatterers. For homogeneously distributed Rayleigh scatterers, $\beta \approx \frac{2}{15}$. We can calculate the sum of the averages over N in (28), by writing:

$$\sum_{i=1}^{N}\langle f(r_i)\rangle = N\int\langle f(r_i)\rangle\rho_s(r)dr \tag{29}$$

where we use $\langle f(r_i)\rangle$ for the part on the right side of (28) which is summed over. We use the spatial density of diffusion paths $\rho_s(r)$, and replace the sum over N, with an integral over all sample points r. This gives:

$$\langle\Delta\phi_p^2\rangle - \langle\Delta\phi_p\rangle^2 \approx \beta k_0^2 l^* s \bar{\Gamma}_s \tag{30}$$

The phase-shift is then a function of transport mean free path l^*, photon path-length s, and $\bar{\Gamma}_s$. The latter represents the spatial convolution integral of the deformation field and spatial density of diffusion paths. It is given by:

$$\bar{\Gamma}_s = \int\rho_s(r)\Big(\langle(\nabla\cdot u_i)^2\rangle + 2\sum_{m,n}\langle\varepsilon_{mn}^2(r_i)\rangle\Big)dr \tag{31}$$

For an incompressible medium, the divergence of the displacement field is zero, $\nabla \cdot u_i = 0$. In that case, the only remaining term is the strain tensor. We can write the electric field correlation function for a system exhibiting a deformation field as:

$$g_1(\tau) = \int_0^\infty P(s) exp[-\gamma k_0^2 l^* s \bar{\Gamma}_s] ds \tag{32}$$

with $\gamma = \beta/2 \approx 1/15$. For cases where there is both Brownian motion and a deformation field, we can write the general expression for the auto-correlation function:

$$g_1(\tau) = \int_0^\infty P(s) exp\Big[-\frac{k_0^2}{3}\frac{s}{l^*}\bar{\Gamma}_B - \gamma k_0^2 l^* s \bar{\Gamma}_s\Big] ds \tag{33}$$

Equation (33) includes both the contribution of Brownian motion $\bar{\Gamma}_B$, and that of a deformation field $\bar{\Gamma}_s$, to the measured de-correlation.

Photon density distribution in scattering media: In spatially-resolved Laser Speckle Imaging, $g_1(\tau)$ and $g_2(\tau)$ are measured for each detection pixel by analyzing the temporal fluctuations in speckle intensity. Interpreting these experimental autocorrelation functions in terms of the internal dynamics of the sample requires solving (33), which is often not possible directly. To arrive at a better understanding of how to interpret experimentally obtained correlation functions in terms of the diffusive and ballistic dynamics of the material under study, we must first understand the path-length distribution, $P(s)$, and the spatial density of diffusion paths, $\rho_s(\mathbf{r})$. To this end we use the diffusion approximation and a random walk model.[24] We start by defining $P_{s,n}(r; r_0, r_d)$ as the probability for a random walk of length s, starting from r_0 and ending at r_d, to pass point r after a distance n. Since the random walk from r_0 through r to r_d consists of two random walks, from r_0 to r and then from r to r_d, we can write:

$$P_{s,n}(r; r_0, r_d) = \frac{G(r_0, r, n) G(r, r_d, s-n)}{G(r_0, r_d, s)} \tag{34}$$

Here, $G(r_0, r, n)$ is the Green's function of a random walk of length n, from r_0 to r. In this context, the Green's function characterizes the reaction of a sample to light. Mathematically, it describes the response of the diffusion equation to an impulse. By extension, the Green's function denotes the statistical weight of a random walk. In order to integrate (34) over all points r in the sample, we can use the Markov property. By treating a random walk as a Markov chain, we assume that its conditional probability distribution depends only on the present state, and not the sequence of events preceding or following it. We integrate (33) over r, and the Markov property enables us to write:

$$\int G(r_0, r, n) G(r, r_d, s-n) dr = G(r_0, r_d, s) \tag{35}$$

so that the integral of the left side of (33) is normalized:

$$\int P_{s,n}(r; r_0, r_d) dr = 1 \tag{36}$$

This corresponds to the notion that the total probability of a photon entering the sample at r_0 and reaching any point r before exiting at r_d is one. We integrate $P_{s,n}(r; r_0, r_d)$ over all n, where $0 < n < s$, and obtain:

$$\rho_s(r; r_0, r_d) = \frac{1}{s}\int_0^s P_{s,n}(r; r_0, r_d) dn \tag{37}$$

$$= \frac{\int_0^s G(r_0, r, n) G(r, r_d, s-n) dn}{s G(r_0, r_d, s)} \tag{38}$$

$$= \frac{1}{s G(r_0, r_d, s)} L^{-1}\left[\tilde{G}(r_0, r, p)\tilde{G}(r, r_d, p)\right] \tag{39}$$

Here, $\tilde{G}$ denotes the Laplace transform of G with respect to n, and corresponding Laplace variable p, and L^{-1} denotes the inverse Laplace transform. The integral in the numerator of (38) is re-written as the inverse Laplace transform term in (39). We use the Laplace transform because it allows us to decompose the statistical weight of the product of the Green's functions in this integral into exponential contributions in a simplified way. By formulating the integral in the Laplace domain, we can solve it using polynomial equations, instead of having to solve linear differential equations. Taking the inverse Laplace transform, we obtain the result in the time domain. Note that $\rho_s(r; r_0, r_d)$ is normalized:

$$\int \rho_s(r; r_0, r_d) dr = 1 \tag{40}$$

We can write the weight of all walks of length s ending at r_d as:

$$G(r_d,s) = \int G(r_0,r_d,s)dr_0 \tag{41}$$

and the distribution of path lengths ending at r_d as:

$$P(r_d,s) = \frac{G(r_d,s)}{\int_0^\infty G(r_d,s)ds} \tag{42}$$

For homogeneous plane illumination in LSI, we can calculate the spatial density of diffusion paths $\rho_s(r;r_d)$, by integrating over over all photon entry points r_0. This gives:

$$\rho_s(r;r_d) = \int \rho_s(r;r_0,r_d)dr_0 \tag{43}$$

$$= \frac{\int_0^s G(r,n)G(r,r_d,s-n)dn}{sG(r_d,s)} \tag{44}$$

$$= \frac{1}{sG(r_d,s)} L^{-1}\left[\tilde{G}(r,p)\tilde{G}(r,r_d,p)\right] \tag{45}$$

The propagator, $G(r_0,r,n)$, gives the probability amplitude of a path from entry point r_0 to point r, with a path-length n. It is the solution of the diffusion equation:

$$\frac{\partial G}{\partial t} = D_L \nabla^2 G \tag{46}$$

Here, $D_L = \frac{c' l*}{3}$ is the diffusion coefficient of photons in the sample, with light speed $c' = \frac{c}{n_m}$, and n_m is the medium refractive index. Since the path length $n = c't$, we can also write this as

$$\frac{\partial G}{\partial n} = \frac{l*}{3} \nabla^2 G \tag{47}$$

The boundary conditions for this equation are defined as:

$$G(r_0, z = 0, n) = 0 \tag{48}$$

$$G(r_0, z = L, n) = 0 \tag{49}$$

This means that the statistical weight of a path starting at r_0, and reaching either the front or back boundary of the sample ($z = 0, L$) at any step n, where $n < s$, is zero. The corresponding initial condition is:

$$G(r_0, r, 0) = \delta(r - r_0) \tag{50}$$

Here we assume that the random walk starts when the photon has penetrated a depth of one transport mean free path into the sample, so we write $r_0 = (x_0, y_0, l^*)$. We also assume that the sample is isotropic and that the x, y and z directions are uncorrelated, so that $G(r)$ can be decomposed in $G(r) = G_x(x)G_y(y)G_z(z)$.

We will now derive an equation for the path-length distribution $P(s)$ of a semi-infinite slab, $L \to \infty$. In this case, the solution of the diffusion equation for the Green's function can be found by the method of images.[28] This consists of mathematically decomposing the physical boundary of the sample into negative and positive photon sources, placed outside and inside the sample, respectively. This creates a set of extrapolated boundaries, with different contributions to the photon flux crossing the real physical boundary. This enables us to solve the diffusion equation for a system where light is crossing the physical barrier of a sample. For a system where light is impinging on the (x,y) plane, and z is the depth, the result is:

$$G(r_0,r,n) = \left(\frac{3}{4\pi n l*}\right)^{\frac{3}{2}} exp\left(-\frac{3[(x-x_0)^2 + (y-y_0)^2]}{4nl*}\right) \tag{51}$$

$$\cdot \left[exp\left(-\frac{3(z-l*)^2}{4nl*}\right) - exp\left(-\frac{3(z+l*)^2}{4nl*}\right)\right] \tag{52}$$

The starting depth of the path is $z_0 = l^*$. For path lengths much longer then l^*, corresponding to the multiple-scattering limit, the z-dependent terms can be expanded in l^*:

$$G(r_0,r,n) \approx 4\pi l^* z\Big(\frac{3}{4\pi n l*}\Big)^{\frac{5}{2}} exp\Big(-\frac{3[(x-x_0)^2+(y-y_0)^2+z^2]}{4nl*}\Big) \tag{53}$$

For homogeneous illumination, we can find the weight of all paths of length s that leave the sample at $r_d = (x_d, y_d, l^*)$ by integrating over all entry points x_0 and y_0:

$$G(r_d,s) = \int_{-\infty}^{\infty}\int_{-\infty}^{\infty} G(r_0,r_d,s)dx_0dy_0 \tag{54}$$

$$= \frac{3}{2}\left(\frac{3l*}{\pi}\right)^{\frac{1}{2}} s^{-\frac{3}{2}} exp\left(-\frac{3l*}{4s}\right) \tag{55}$$

Then, the distribution of path lengths ending at an exit point r_d is:

$$P(r',s) = P(s) = \frac{G(r_d,s)}{\int_0^{\infty} G(r_d,s)ds} \tag{56}$$

$$= \left(\frac{3l*}{\pi}\right)^{\frac{1}{2}} s^{-\frac{3}{2}} exp\left(-\frac{3l*}{4s}\right) \tag{57}$$

The path-length distribution $P(s)$, given by (57), is a function of the transport mean free path. In this model, it is independent of the degree of inhomogeneity in the sample.

In a homogeneous, non-deformed sample, the mean squared displacement is equal throughout the sample. Then, (21) gives the thermal part of de-correlation:

$$\bar{\Gamma}_B = \langle \Delta r(t)^2 \rangle \int \rho_s(r)dr = \langle \Delta r(t)^2 \rangle \tag{58}$$

It is evident that the contribution of Brownian motion to de-correlation is independent of the probed sample locations, r. Equation (20) then corresponds to a Laplace transform of $P(s)$, with Laplace variable $p = k_0^2 \frac{\langle \Delta r(t)^2 \rangle}{3l^*}$. The Laplace transform of $P(s)$ is:

$$L[P(s)] = \int_0^{\infty} P(s)e^{-ps}ds = e^{-\sqrt{3l^*p}} \tag{59}$$

The electric field correlation function for a homogeneous, Brownian sample can then be written as:

$$g_1(\tau) = exp\Big(-\sqrt{k_0^2\langle \Delta r(\tau)^2 \rangle}\Big) \tag{60}$$

This expression for $g_1(\tau)$ is normally used to obtain the mean-squared displacement from a LSI correlation measurement.[10] For inhomogeneous samples with broken structural or dynamical symmetry, the measured de-correlation depends on the distribution of probed sample locations r. In this case, the contribution of a deformation field is given by $\bar{\Gamma}_s = 2\sum_{m,n} \varepsilon_{mn}^2$. We can illustrate this by considering a sample experiencing a shear deformation in one direction, i.e. $\varepsilon_{xz} = \varepsilon$, with all other components of the strain tensor equal to zero. Then the field correlation function is expressed using (33), as:

$$g_1(\tau) = exp\Big(-k_0\sqrt{\langle \Delta r(t)^2 \rangle + 3(l^*)^2\gamma\varepsilon^2}\Big) \tag{61}$$

The first term under the square root is the contribution of Brownian fluctuations, while the second term originates from the deformation field. For cases involving steady shear flow, we work with the strain rate tensor, and we define $\varepsilon = \dot{\gamma}t$.

3.1 Theory and Monte-Carlo comparison: In order to validate our derivation of the path-length distribution, we ran a Monte-Carlo simulation and compared the results with theory. We chose a homogeneous system, where $P(s)$ and $\rho_s(z)$ are given by (57) and (43), respectively. We simulated light propagation in a homogeneous diffusive sample for 6 wavelengths in the visible and near-IR regime, assuming plane-illumination, and calculated the photon density distribution for the depth direction, i.e. the z-axis. The script would choose a photon entry point (x,y) on the slab, and simulate a random walk starting

at a depth of l^*. The path had a step-length which was randomly chosen from a Gaussian distribution centered around the transport mean free path, l^*. We used a multiple-scatter detection condition, and photons included in the statistics had to have a path-length which matched a preset value. In our case, the requirements were a minimum of 10 scattering events, and a path-length of 30 mean free paths. Since the step-lengths were chosen randomly from a Gaussian distribution, we allowed a $\pm 0.5\%$ deviation for the path-length condition. Boundary effects were avoided by choosing a sufficiently large system size, $L > \frac{s}{2l^*}$. We compared the intensity distributions obtained analytically using $F(z) = P(s)\rho_s(z)$, with the results enumerated using Monte-Carlo simulations in the classical limit. Figure 4 shows the probability density distribution as a function of sample

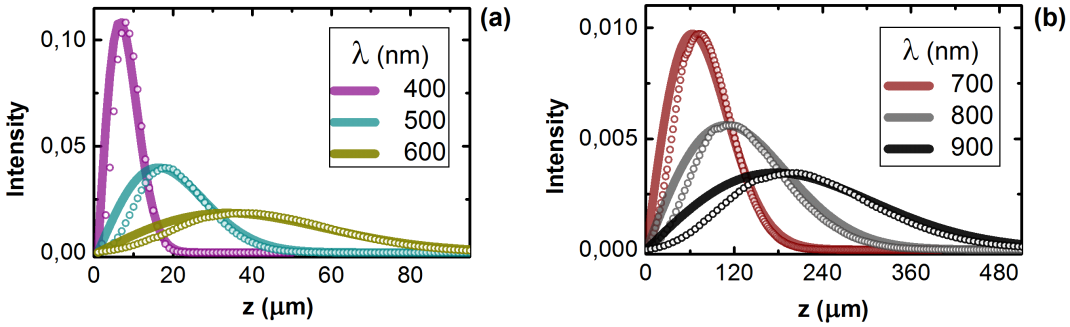

Figure 4. Comparison of analytical and Monte-Carlo results for the backscatter density distribution of a diffusive, homogeneous sample in the Rayleigh regime. The integral of the analytical results is normalized to one. **(a)** Intensity as a function of sample depth, for $\lambda = 400, 500, 600\,nm$. **(b)** Intensity as a function of sample depth, for $\lambda = 700, 800, 900\,nm$.

depth, for $\lambda = 400 - 900\,nm$. The maximum penetration depth, as well as the contribution of large depths to back-scattering, both increase proportionally to the transport mean free path, and by extension to wavelength. Characteristically for each wavelength, the probability density reaches it's maximum at a depth of several transport mean free paths, and then gradually reduces back to zero. This is in line with the expectations.

4. LSI in inhomogeneous systems

LSI is often used to probe spatial inhomogeneities and internal dynamics in complex, turbid systems. When dynamic processes with more than one characteristic time-scale are present in a sample, LSI measurements will be affected by spatial convolution of the photon distribution profile and structural parameters of the sample. A practical example of this process is blood-flow imaging. The diffusive dynamics of the tissues above the vessel, the diffusive and convective dynamics within the blood vessel, and possible mechanical deformations due to tissue contractions, all convolve to give rise to a final 2-dimensional LSI image. The extent to which these different dynamics contribute to the observed dynamical decorrelation of the speckle pattern, depends strongly on the intensity and path length distribution of photons probing the material. To understand these effects, we will consider several scenarios. We will start by formulating expressions for the spatial density of diffusion paths $\rho_s(r)$, for systems inhomogeneous in one or a combination of (x,y,z) axes. It will be assumed that (x,y) is the imaging plane, and z is the depth axis.

Inhomogeneous in (x): In this case, only the x-dependence of the Greens function (51) is needed:

$$G_x = G(x,x_d,n) = \Big(\frac{3}{4\pi n l^*}\Big)^{\frac{1}{2}} exp\Big(-\frac{3(x_d-x)^2}{4nl^*}\Big) \tag{62}$$

The total probability of a path going from a point x in the sample to any exit point x_d after a distance n is 1: $G(x,n) = \int G(x,x_d,n)dx_d = 1$. From (43) it then follows that the corresponding spatial density of diffusion paths for a sample inhomogeneous in the x-direction is:

$$\rho_s(x,x_d) = \frac{1}{s}\int_0^s G(x,x_d,n)dn \tag{63}$$

$$= \sqrt{\frac{3}{\pi s l^*}} exp\Big(-\frac{3\Delta x^2}{4sl^*}\Big) - \frac{3\sqrt{\Delta x^2}}{2sl^*} Erfc\Big(\sqrt{\frac{3\Delta x^2}{4sl^*}}\Big) \tag{64}$$

where $\Delta x = x_d - x$.

Inhomogeneous in (x,y): If a sample is inhomogeneous in the(x,y) direction, but homogeneous in z, we can integrate out the z-dependence of $G(r_0,r,n)$ and we only need $G(\rho,\rho_d,n) = G_xG_y$:

$$G(\rho,\rho_d,n) = \Big(\frac{3}{4\pi nl^*}\Big)exp\Big(-\frac{3(\rho_d-\rho)^2}{4nl^*}\Big) \tag{65}$$

with $\rho = (x,y)$. Also in this case, $G(\rho,\rho_d,n)$ is normalized over all exit points ρ_d, so that $\int G(\rho,\rho_d,n)d\rho_d = 1$. Using (43), we write the spatial density of diffusion paths for a sample inhomogeneous in the (x,y) direction as:

$$\rho_s(\rho,\rho_d) = \frac{1}{s}\int_0^s G(\rho,\rho_d,n)dn \tag{66}$$

$$= \frac{3}{4\pi sl^*}E_1\Big(\frac{3(\rho_d-\rho)^2}{4sl^*} \tag{67}$$

Here, $E_1(x)$ is the exponential integral:

$$E_1(x) = \int_x^\infty \frac{e^{-t}}{t}dt \tag{68}$$

Inhomogeneous in (z): We will now invert the situation, and consider a system homogeneous in (x,y), but inhomogeneous in z. We integrate out the (x,y)-dependence and obtain:

$$G(l^*,z,n) = 4\pi l^* z\Big(\sqrt{3}4\pi nl^*\Big)^{\frac{3}{2}}exp\Big(-\frac{3z^2}{4nl^*}\Big) \tag{69}$$

Using (43) and the Laplace transform of (69), we find for the spatial density of diffusion paths:

$$\rho_s(z) = \frac{6z}{sl^*}exp\Big(-\frac{3z^2}{sl^*}\Big) \tag{70}$$

Inhomogeneous in (x,y,z): Finally, for systems inhomogeneous in (x,y,z), we use all parts of the Green's function and write:

$$\rho_s(r;r_d) = \frac{1}{sG(r_d,s)}L^{-1}\Big[\tilde{G}(r,p)\tilde{G}(r,r_d,p)\Big] \tag{71}$$

with $G(r_d,s)$ given by (53) and $G(r,n)$ written as:

$$G(r,n) = \int_{-\infty}^{\infty}\int_{-\infty}^{\infty} G(r_0,r,s)dx_0dy_0 \tag{72}$$

$$= \frac{3}{2}\Big(\frac{3}{\pi l^*}\Big)^{\frac{1}{2}}zn^{-\frac{3}{2}}exp\Big(-\frac{3z^2}{4nl^*}\Big) \tag{73}$$

The Laplace transform of this is:

$$\tilde{G}(r,p) = 3exp\Big(-\sqrt{\frac{3pz^2}{l^*}}\Big) \tag{74}$$

The Laplace transform of $G(r,r_d,n)$, written in the form of (53), is:

$$\tilde{G}(r,r_d,p) = \frac{3}{2\pi}\frac{z}{|\Delta\rho|^3}\Big(\sqrt{\frac{3p\Delta\rho^2}{l^*}}+1\Big)exp\Big(-\sqrt{\frac{3p\Delta\rho^2}{l^*}}\Big) \tag{75}$$

with $\Delta\rho^2 = (x-x_0)^2+(y-y_0)^2+z^2$. Substitution in the expression for $\rho_s(r)$ and carrying out the inverse transformation leads to:

$$\rho_s(r,r_d) = \frac{3}{2\pi l^*}\frac{z}{\Delta\rho^2}\Big[\frac{3(z+|\Delta\rho|)^2}{2s^2l^*}+\frac{z}{|\Delta\rho|s}\Big]exp\Big(-\frac{3((z+|\Delta\rho|)^2-(l^*)^2)}{4sl^*}\Big) \tag{76}$$

The field autocorrelation function, $g_1(\tau)$, can be calculated from (33), provided that the spatial distribution of diffusion coefficients is known. The path-length probability function $P(s)$, is given by (57), and the weighted mean-squared displacement due to Brownian motion and deformation field are given by equations (21) and (31), respectively. Depending on the degree of

inhomogeneity of a sample, suitable expressions for the spatial density of diffusion paths may be chosen from (64), (67), (70), and (76).

4.1 Simulation of LSI measurements: In this section, we will show how LSI measurements on non-strained, turbid samples are affected by the presence of structural inhomogeneities, and by having dynamic internal processes with different characteristic time-scales. We will do this for 2 types of samples. In case (A), a flowing layer is embedded at different depths in a diffusive slab, with its surface parallel to the imaging plane. This represents a system inhomogeneous in the z-axis. Here, we will show how the field correlation function $g_1(\tau)$, and the mean-squared displacement $\langle \Delta r(r,\tau)^2 \rangle$, depend on the depth and thickness of the flowing layer. We will also illustrate how changing the exponential decay time constant, τ, leads to wavelength-dependent non-linear effects on the field correlation function. In case (B), the surface of the flowing layer is orthogonal to the imaging plane, and is inhomogeneous in the x-axis. For this system, only layer thickness is varied. We will show how a LSI measurement depends on the ratio of transport mean free path and layer thickness, and how large transport mean free paths in samples with small-scale inhomogeneities lead to resolutional blurring of LSI images.

We start by defining the characteristic dynamic processes of our system. First, we calculate mean-squared displacement values for a range of τ's for the flowing layer and the diffusive slab (Figure 5a). The flowing layer exhibits Brownian motion, as well as convective motion, so that the mean-squared displacement is given by $\langle \Delta r(r,z)^2 \rangle = 6D\tau + v^2\tau^2$. The surrounding of the layer exhibits only Brownian motion, and here we use only the diffusive part. The diffusion coefficient of the surrounding matrix was chosen two orders of magnitude smaller than that of the convective layer, in order to approximate a relatively static environment, or one whose characteristic time-scales are significantly longer. We can see that for longer τ's, the contribution

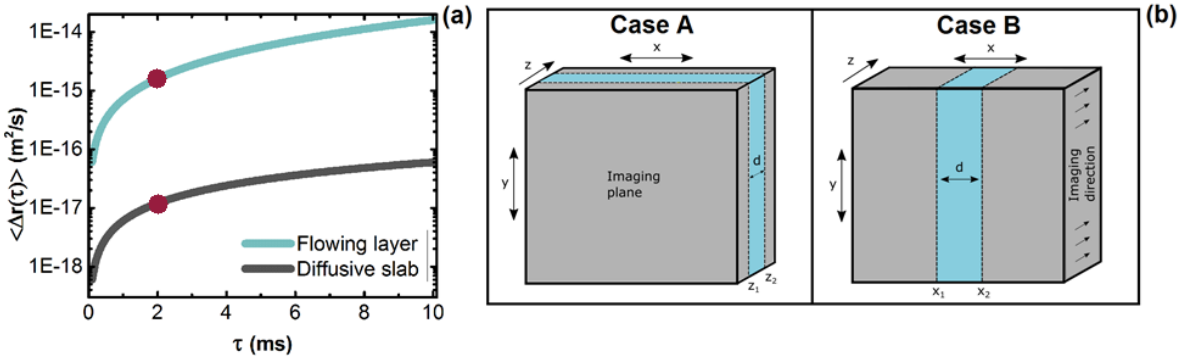

Figure 5. **(a)** Mean-squared displacement as a function of exponential decay time constant τ, for a diffusive slab exhibiting only Brownian motion, and a flowing layer exhibiting both Brownian motion and convection. The red data-points represent the mean-squared displacements corresponding to $\tau = 2$ ms, as chosen for simulations. **(b)** Orientations of the flowing layer relative to the imaging direction used for simulation. The imaging plane in both conformations is the (x,y) plane. z is the depth axis of the samples. The layer thickness is denoted by d. (z_1,z_2) and (x_1,x_2) are the start-end coordinates of the layers in cases A and B, respectively.

of short time-scale behavior, such as convection, to the measured mean-squared displacement increases faster than for the diffusive part. We have chosen a constant τ for all simulations, $\tau = 2\,ms$, except for those studying the effect of τ on $g_1(\tau)$. At this τ, the input mean-squared displacement of the layer and bulk were 1.6e-15 and 1.2e-17 m^2/s, respectively. With our choice of sample parameters, the contribution of convection to the de-correlation is higher than that of Brownian motion. However, at such short τ, self-correlation of the convective region is still present, and the contrast with the Brownian region is reduced. Choosing a longer τ will increase the contribution of convection to the de-correlation, more significantly than it will increase that of Brownian motion. This will reduce the measured self-correlation in the convective region, increasing the imaging contrast.

(Case A) Decorrelation in z-inhomogeneous systems: Figure 6 shows the results of a simulated LSI measurement for a sample inhomogeneous in z. (a,b) shows the field correlation function and mean-squared displacement plotted against transport mean free path, for flowing layers of varying thickness, but with a constant end-depth, z_2. To model this, we used (57) and (70) for the path-length probability function and the spatial density of diffusion paths, respectively. The field correlation function was then calculated with (20). To obtain the mean-squared displacement from $g_1(\tau)$, we used a fitting procedure described in[10]. When layer thickness is reduced by increasing z_1 at constant z_2, the minimum of $g_1(\tau)$ increases in magnitude and

exhibits a shift to lower transport mean free paths. This can be explained by the fact that a thin layer contributes less to the de-correlation, because photons spend less time traveling within it. Wavelengths with large transport mean free paths will have a lower probability of a random walk localized within a thin layer. They will be less likely to probe the layer to a sufficient extent, than wavelengths whose transport mean free path is smaller or on the order of the layer thickness. Consequently, for layers with increasing z_1 and constant z_2, the magnitude of the measured correlation will increase, and the minimum of $g_1(\tau)$ will be displaced to lower l^*. In (c,d), the field correlation function and mean-squared displacement are plotted against transport mean free path, for a layer of constant thickness $d = 50um$, located at different depths within the slab. As the layer is positioned at increasing depth, the magnitude of the correlation increases, and the minimum of $g_1(\tau)$ is shifted to higher transport mean free paths. This is reasoned by the fact that, since the layer thickness does not change, all transport mean free paths will have a constant photon density distribution within the layer. In this case, the measured de-correlation will depend only on the probability of a photon reaching the depth of the layer. This is why, when the layer is shifted to larger depths, the measured correlation increases, and the minimum of $g_1(\tau)$ is displaced to larger l^*. Looking at these two cases, it is evident that for a generalized z-inhomogeneous system like this, there is an interplay between different effects giving rise to the de-correlation measured with LSI. Both the probability of a photon reaching the layer depth, and the ratio of transport mean free path to layer thickness, determine the effective contribution to the measurement. For the first example, where z_1 is increased at constant z_2, we see that the effect of reduced layer thickness is more significant than that of the layer being located at increasing starting depths z_1. The measured correlation still increases, as in the second case, but the minimum of $g_1(\tau)$ is displaced to smaller l^*. For the mean-squared displacement profiles, the quantitative results range between the two input values.

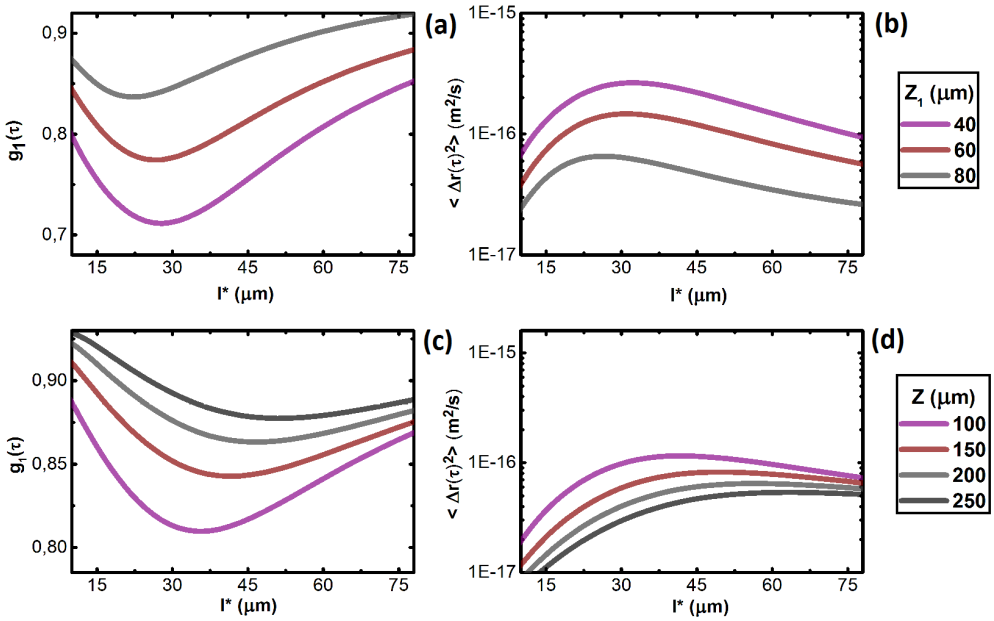

Figure 6. LSI measurements on a z-inhomogeneous system. Input mean-squared displacements for the layer and surrounding slab are $1.2 \cdot 10^{-17}$ and $1.6 \cdot 10^{-15}$ $\frac{m^2}{s}$, respectively. **(a,b)** Field correlation function and mean-squared displacement plotted against transport mean free path, for three convective layers with varying z_1 and $z_2 = 100um$; **(c,d)** Same as in (a,b), for a convective layer of constant thickness, $d = 50um$, placed at increasing depth (z_1, z_2). For small l^*, the extrapolated boundary condition does not hold, resulting in mathematical artifacts. Therefore, data for $l^* < 10\,um$ were omitted from the plot.

In addition to sample structure and imaging wavelength, the extent to which spatial convolution of LSI measurements occurs depends also on the exponential decay time constant, τ. As illustrated in figure 5(a), changing the characteristic time-scale of a measurement by varying τ, will alter the mean-squared displacement of the diffusive and convective parts to a different extent, and by extension affect their contribution to the measured de-correlation. To study this effect, we simulated a z-inhomogeneous sample with three convective layers of constant thickness, $d = 10um$, positioned at increasing depth (z_1, z_2). Figure 7(a-c) shows the correlation measurement as a function of τ, for three wavelengths in the visible spectrum. As expected, when τ is increased, the correlation is reduced. However, it is evident that this decrease is non-linear, and varies for different layer depths, as well as for wavelengths. In (a), where the layer is located close to the imaging plane, this reduction is most expressed for 600nm. We see that initially, at low τ, the measured correlation is higher for 600nm than for 400nm.

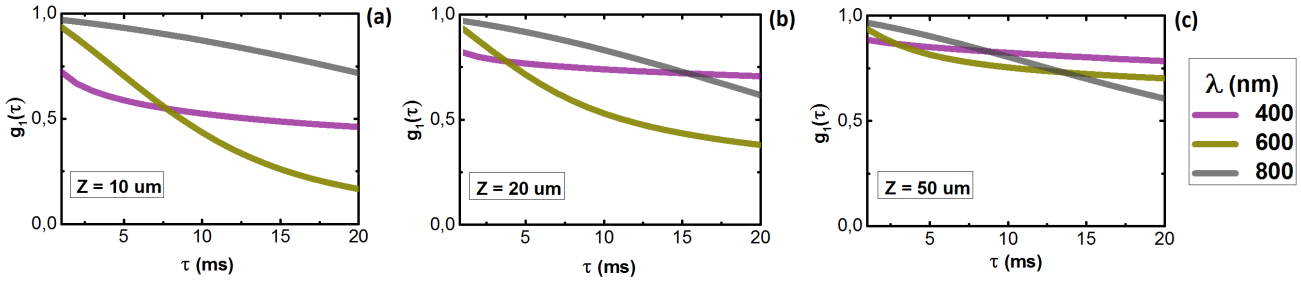

Figure 7. **(a-c)** Electric field correlation function plotted against τ for a 10*um* thick layer positioned at increasing depth z.

However, at higher τ, the contribution of the flowing layer to the de-correlation becomes more significant. Consequently, measurements conducted with an imaging wavelength whose photon density is high near the layer will be most affected. As the layer is displaced to a larger depth, as in (b) and (c), the difference between 400 and 600nm becomes smaller. The reduction is then more expressed for 800nm, whose photon distribution profile maximum starts overlapping with the layer location.

(Case B) Resolutional blurring in x-inhomogeneous systems: In addition to systems inhomogeneous in z, we also investigated LSI measurements in systems which are inhomogeneous in x. This corresponds to the right side of figure (5b). Figure 8(a-c) shows the measured mean-squared displacement as a function of pixel position on the x-axis, for convective layers of increasing thickness. In (a), long wavelengths are unable to display a clear mean-squared displacement profile. This is because a large transport mean free path permits probing a larger total sample volume, thereby reducing the contribution of the layer to the measurement. As the transport mean free path becomes smaller such that eventually $d > l^*$, as in (b) and (c), the resolution increases. Looking at figure (8) from a quantitative perspective, we see that short wavelengths probe the layer more significantly for pixels localized near the layer, measuring a higher mean-squared displacement with better resolution. Longer wavelengths, despite having a lower resolution, probe the flowing layer more significantly than shorter wavelengths for increasing layer-pixel distances. At longer distances, they have a higher contribution of the flowing layer to the de-correlation, and measure a higher mean-squared displacement. It is also evident that, as the layer thickness increases, the difference in mean-squared displacement measured with different wavelengths becomes smaller within the layer. This is because in that case, also the wavelengths with a high transport mean free path can probe the layer to a sufficient degree.

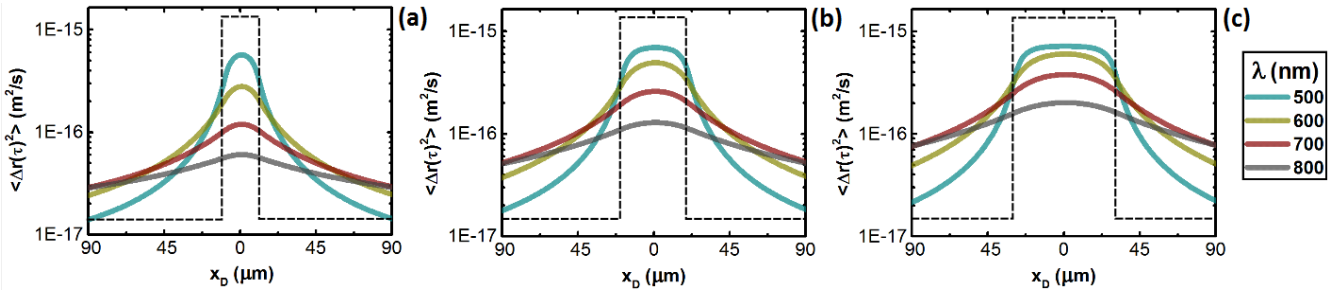

Figure 8. Mean-squared displacement as measured with LSI, plotted against detector pixel position on the x-axis, for $\lambda = 500, 600, 700$, and 800 nm. Input mean-squared displacements for the layer and surrounding slab are $1.2 \cdot 10^{-17}$ and $1.6 \cdot 10^{-15}$ $\frac{m^2}{s}$, respectively. **(a,b,c)** Mean-squared displacement profile for a 20,40, and 60 um thick convective layer, respectively. The dotted lines represent the real profile of the layer-slab systems.

5. Discussion

In the previous sections, we have presented a theoretical model describing how various dynamical processes converge with structural information of a turbid sample, to give fluctuating speckle patterns as measured with LSI. we validated Rayleigh scattering theory with regards to its predictions of the mean free path dependence on imaging wavelength. Based on this, we presented a derivation of the quantities making up the electric field correlation function $g_1(\tau)$, namely the path-length distribution $P(s)$, and

the spatial density of diffusion paths $\rho_s(r)$. We calculated the photon density distribution for a homogeneous, semi-infinite slab, and verified this with a Monte-Carlo simulation. Finally, we simulated LSI measurements on two spatially different inhomogeneous systems, consisting of various conformations of a flowing layer embedded in a diffusive slab. The LSI simulation results give insight into the variation of the field correlation function, and the mean-squared displacement, when measured with different wavelengths. It is shown that, for an inhomogeneous sample, the contribution of a region within the sample to the field correlation function depends on the degree of inhomogeneity, the location of the inhomogeneity relative to the imaging plane, and the exponential decay time constant. The effect of sample structure on the photon distribution profile is reflected in the spatial density of diffusion paths, $\rho_s(r)$, which takes different forms, depending on the shape and location of the inhomogeneous region within the sample. The probability of a photon reaching the location of an inhomogeneity depends on the path-length distribution, $P(s)$. However, we see also that upon reaching the inhomogeneity, the probability of a photon sufficiently probing that layer before being detected depends on the ratio between transport mean free path and layer thickness. Furthermore, variation of the exponential decay time constant affects the mean-squared displacement of ballistic and diffusive origin to a different extent, which is subsequently reflected in the measured correlation. Besides interesting qualitative insight, the LSI simulations exhibit quantitative accuracy as well. For both case (A) and (B), the calculated mean-squared displacement profiles display a transport mean free path dependent band of values, ranging between the input values of the convective layer and diffusive matrix.

Extended with a suitable de-convolution method, this model forms the basis for development of 3D LSI technology, which will open up the door to high-definition, depth-resolved LSI imaging. This will have direct applications in bio-medicine, materials science, and other domains where LSI is already used. With the possibilities of LSI mind, it should be noted that accurate, quantitative LSI measurements still present a challenging task. There are several practical and fundamental issues that need attention, before the full potential of LSI can be utilized. For one, significant progress has to be made with regards to developing calibration-free, quantitative LSI methods. Furthermore, implementation of accurate and efficient algorithms for real-time LSI measurements, such as in laser speckle correlation imaging (LSCI), is largely still in experimental stages. Finally, we note that our model uses several approximations which are sometimes not satisfied by real systems. Whereas we have assumed a constant transport mean free path throughout the sample, in real inhomogeneous systems this is often not so. Therefore, future research should focus on investigating photon distribution profiles in structurally more complex systems, with different characteristic time-scales of dynamic processes, and having regions of different mean free path distributions.

6. Methods

Validation of Rayleigh theory: to verify the wavelength dependence of the transport mean free path in the Rayleigh regime, we measured the radial enhanced back-scatter cone decay of a turbid, diffusive sample. we used a $\phi = 0.45\frac{w}{w}$ polystyrene-butylacrylate (79:21) suspension with a particle size of 70.3 ± 0.78 nm, determined with dynamic light scattering. Absorption of polystyrene at these wavelengths is on the order of $< 10^{-5}$, and has been neglected.[29] We used a radial profile angle function to calculate a radial intensity decay curve from the snapshots. From the decay curve, we determined the transport mean free paths of the corresponding wavelengths. The fitting procedure is described in[30]. For theory calculations, the wavelength-dependence of refractive index of particle and water was accounted for using formulas obtained from literature.[31] To satisfy ergodic criteria and to ensure proper averaging over all fluctuation patterns, we acquired sufficient snapshots, with intervals on the order of the decorrelation time. Micro-Manager was used for image acquisition,[32] and Matlab for data analysis.[33] The light-source was a Thorlabs MCLS1 4-channel laser box, and the camera was a Hamamatsu 9100-13 single-photon camera.

LSI theory and numerical simulations: derivation of analytical solutions to the path-length distribution $P(s)$, the spatial density of diffusion paths $\rho_s(r)$, and the electric-field correlation function $g_1(\tau)$ was done with Mathematica.[34] Numerical results were obtained with Matlab.[33] Parameters used to simulate the dynamic processes of the flowing layer were obtained from literature.[35,36]

7. Conclusion

The physics of photon propagation in multiple scattering, inhomogeneous systems, represents complex and indeterminate processes which are challenging to model. This study presents a theoretical framework that explains how internal dynamic processes and structural parameters convolve, to give rise to speckle fluctuation patterns as measured in LSI. By extending the model used for analysis of speckle patterns to structurally inhomogeneous samples, it is demonstrated that improved accuracy and higher resolution can be achieved in LSI, by analyzing speckle correlations within a framework of more complicated turbid systems. Development of suitable de-convolution techniques, combined with detailed models of photon statistics in inhomogeneous media, will allow these insights to be put into practice. This will result in the development of 3D LSI technology, and realize the full potential of laser speckle imaging.

References

1. Briers, D. *et al.* Laser speckle contrast imaging: theoretical and practical limitations. *Journal of Biomedical Optics* **18**, 66018 (2013).
2. Boas, D. A. & Dunn, A. K. Laser speckle contrast imaging in biomedical optics. *J Biomed Opt.* **15**, 011109 (2010).
3. Nadkarni, S. K. *et al.* Characterization of atherosclerotic plaques by laser speckle imaging. *Vascular Medicine* **112**, 885–892 (2005).
4. Regan, C. *et al.* Fiber-based laser speckle imaging for the detection of pulsatile flow. *Lasers in Surgery and Medicine* **47**, 520–525 (2015).
5. Nemati, M. *et al.* Application of full field optical studies for pulsatile flow in a carotid artery phantom. *Biomedical Optics Express* **6**, 4037–4050 (2015).
6. Humeau-Heurtier, A., Guerreschi, E., Abraham, P. & Mahe, G. Relevance of laser doppler and laser speckle techniques for assessing vascular function: State of the art and future trends. *IEEE transactions on bio-medical engineering* **60** (2013).
7. Young, A. & Vishwanath, K. Quantitative assessment of reactive hyperemia using laser speckle contrast imaging at multiple wavelengths. *Proc. SPIE 9707, Dynamics and Fluctuations in Biomedical Photonics XIII* **97071H** (2016).
8. Thakor, N. V. Neurophotonics by laser speckle and photoacoustic imaging. *2016 International Conference on Optical MEMS and Nanophotonics (OMN)* 1–2 (2016).
9. Vaz, P. G., Humeau-Heartier, A., Figueiras, E., Correia, C. & Cardoso, J. Laser speckle imaging to monitor microvascular blood flow: a review. *IEEE Reviews in Biomedical Engineering* **9**, 106–20 (2016).
10. van der Kooij, H. M., Fokkink, R., van der Gucht, J. & Sprakel, J. Quantitative imaging of heterogeneous dynamics in drying and aging paints. *Scientific Reports* **6** (2016).
11. Kashany, Z. H. *et al.* Laser speckle micro rheology for micro-mechanical mapping of bio-materials. *Proc. SPIE 9707, Dynamics and Fluctuations in Biomedical Photonics XIII, 970702* **970702** (2016).
12. Alvarado, F. A. P., Hussein, M. A. & Becker, T. Laser speckle spectroscopy image analysis for high pressure and high temperature treatment discrimination on ldpe, hdpe bopp, bopa and pet polymer layers used for food packaging. *Journal of Food Process Engineering* **00**, 00–00 (2015).
13. Basak, K., Dey, G., Mahadevappa, M., Mandal, M. & Sheet, D. Learning of speckle statistics for in vivo and noninvasive characterization of cutaneous wound regions using laser speckle contrast imaging. *Microvascular Research* **107**, 6–16 (2016).
14. Weiner, J. & Ho, T. *Light-Matter Interaction - Fundamentals and Applications (Vol.1)* (2003).
15. van der Mark, M. B., van Albada, M. P. & Lagendijk, A. Light scattering in strongly scattering media: Multiple scattering and weak localization. *Phys. Rev. B* **37** (1988).
16. Goodman, J. W. *Statistical properties of laser speckle patterns* (1975).
17. Irimpan, L., Dann, V., Krishnan, B. & et al. Backscattering of laser light from colloidal silica. *Laser Phys.* **18**, 882 (2008).
18. Berne, B. & Pecora, R. *Dynamic Light Scattering* (1976).
19. Maret, G. & Wolf, P. Multiple light scattering from disordered dedia - the effect of brownian motion of scatterers. *Z. Phys. B - Condensed Matter* **65**, 409–413 (1987).
20. Popescu, G. & Dogariu, A. Optical path-length spectroscopy of wave propagation in random media. *Optics Letters* **24**, 442–444 (1999).
21. Bicout, D. J. & Weiss, G. H. A measure of photon penetration into tissue in diffusion models. *Optics Communications* **158**, 213–220 (1998).
22. Bianco, S. D., Martelli, F. & Zaccanti, G. Penetration depth of light re-emitted by a diffusive medium: theoretical and experimental investigation. *Physics in Medicine and Biology* **47** (2002).
23. Martelli, F. *et al.* There's plenty of light at the bottom: statistics of photon penetration depth in random media. *Scientific Reports* **6** (2016).
24. Bicout, D. & Maynard, R. Diffusing wave spectroscopy in inhomogeneous flows. *Physica A: Statistical Mechanics and its Applications* **199**, 387–411 (1993).
25. Albada, M. P. V. & Lagendijk, A. Observation of weak localization of light in a random medium (1985).

26. Durian, D. J. Influence of boundary reflection and refraction on diffusive photon transport. *Physical Review E* **50**, 857 (1994).

27. Erpelding, M., Amon, A. & Crassous, J. Diffusive wave spectroscopy applied to the spatially resolved deformation of a solid. *Phys. Rev. E* **78** (2008).

28. Lorenzo, J. R. *Principles of diffuse light propagation* (2012).

29. Inagaki, T., Arakawa, E. T., Hamm, R. N. & Williams, M. W. Optical properties of polystyrene from the near infra-red to the x-ray region and convergence of optical sum rules. *Physical Review B* **15**, 3243–3253 (1977).

30. Verma, M., Singh, D. K., Senthilkumaran, P., Joseph, J. & Kandpal, H. C. Ultrasensitive and fast detection of denaturation of milk by coherent backscattering of light. *Scientific Reports* **4** (2014).

31. Thormahlen, I., Straub, J. & Griguli, U. Refractive index of water and its dependence on wavelength, temperature, and density. *J. Phys. Chem. Ref. Data* **14** (1985).

32. Edelstein, A. D. *et al.* Advanced methods of microscope control using umanager software. *Journal of Biological Methods* (2014).

33. Matlab and statistics toolbox release 2012b, the mathworks, inc., natick, massachusetts, united states.

34. Wolfram research, inc., mathematica, version 11.0, champaign, il (2016).

35. KP, I., MK, K. & Yul, L. Blood flow velocity in capillaries of brain and muscles and its physiological significance. *Microvascular Research* **22**, 143–55 (1981).

36. Higgins, J. M., Eddington, D. T., Bhatia, S. N. & Mahadevan, L. Statistical dynamics of flowing red blood cells by morphological image processing. *PLOS Computational Biology* **5** (2009).